Available online at www.sciencedirect.com

SciVerse ScienceDirect

Acta Materialia 61 (2013) 5937–5948

Acta MATERIALIA

www.elsevier.com/locate/actamat

Anisotropic mechanical properties of amorphous Zr-based foams with aligned, elongated pores

Marie E. Cox [a,*], David C. Dunand [b]

[a] National Research Council, Naval Research Laboratory, Washington, DC 20375, USA
[b] Department of Materials Science and Engineering, Northwestern University, Evanston, IL 60208, USA

Received 20 December 2012; received in revised form 13 June 2013; accepted 16 June 2013
Available online 29 July 2013

Abstract

Equal-channel angular extrusion is used to consolidate a blend of amorphous $Zr_{56.3}Nb_{5.1}Cu_{15.6}Ni_{12.9}Al_{10.0}$ and crystalline W powders into dense composites. Chemical dissolution of the crystalline phase results in amorphous foams with elongated pores, aligned at a 22–28° angle with respect to the extrusion direction, whose compressive properties are studied for various orientations. As the angle between the pore long direction and the applied stress direction increases from 0° to 68°, there is a significant decrease in loading stiffness and peak stress, as expected from predictive analytical models; however, the observed increase in stiffness and peak stress observed when the pores are oriented 90° to the direction of loading is not predicted by all of the models. Foams with pores aligned 24–68° to the direction of loading show increased plastic bending in individual walls and accumulation in microscopic damage without failure, leading to increased compressive ductility and absorbed energy over other orientations.

Keywords: Metallic foam; Bulk metallic glass; Equal channel angular press; Zirconium-based glassy alloy; Porous material

1. Introduction

Bulk metallic glasses (BMGs) have high specific strengths but fail catastrophically as a result of their lack of room-temperature plasticity due to highly localized shear bands [1]. To increase the fracture stress and ductility of BMGs, ductile second phases or pores have been added to arrest the shear-band propagation [2–4]. To take advantage of the shear band arrest, porous or foamed alloys based on Pd [5,6], Zr [7–9], Fe [10], Ti [11], La [12], Cu [13] and Mg [14] have been developed using liquid, supercooled liquid or solid-state processing techniques.

Pore orientation has been shown to have an effect on the mechanical properties in low-porosity closed-cell crystalline metallic foams [15] and BMG foams [16]. Wada et al. studied Pd-based BMG foams with closed, aligned, elliptical pores having an aspect ratio of 3 and porosities (pore volume fractions) $p = 3$ and 11%, prepared by quenching in a hydrogen atmosphere followed by a thermomechanical treatment in the supercooled liquid state [16]. The results from compression tests performed on $p = 11\%$ samples with the long axis of the pores oriented parallel and normal to the direction of loading showed an significant effect of pore orientation on the mechanical properties. The sample with pores oriented normal to the loading direction exhibited lower yield strength ($\sigma_y = 1070$ MPa) and higher plastic strain ($\varepsilon_f = 24\%$) than samples with pores parallel to the loading direction ($\sigma_y = 1460$ MPa and $\varepsilon_f = 2\%$). This is attributed to a more severe stress concentration factor for the latter pore orientation, leading to a higher density of shear bands which increases the foam's macroscopic plasticity but decreases its yield strength.

Ide et al. [15] studied the effect of pore orientation on the compressive properties of lotus-type crystalline stainless steels with very high aspect ratio closed-cell pores. The foams ($p = 39\%$) with elongated pores oriented 0–90° to

* Corresponding author. Tel.: +1 8474915370.
E-mail address: dunand@northwestern.edu (D.C. Dunand).

1359-6454/$36.00
http://dx.doi.org/10.1016/j.actamat.2013.06.028

the direction of loading were found to exhibit an almost linear relationship between the yield strength and pore orientation with a reduction in strength of nearly 2 from the 0° to the 90° orientation. The mode of macroscopic deformation was also affected by the pore orientation, with low-angle orientations (pores aligned with loading direction) deforming uniaxially with barreling, high-angle orientations (pores almost normal to the direction of loading) deforming uniaxially without barreling, and the intermediate orientations (28–45° to the direction of loading) deforming by macroscopic shear.

In addition to arresting shear band propagation at the pores, amorphous foams with submillimeter strut dimensions benefit from shear band stabilization, resulting in struts that deform in bending, further increasing the compressive ductility of the foam [17,18]. It has been suggested that amorphous metal struts with a high aspect ratio are preferred for enhanced bending deformation with plasticity compared to pores composed of short equiaxed struts [7,17].

The mechanical properties of four BMG open-cell structures with highly elongated pores have been reported. The first, a Ni-based material processed by warm extrusion of amorphous powders blended with 40 vol.% brass, produced a foam (by removal of the elongated brass phase acting as a space-holder) with highly oriented struts in the direction of extrusion [19]. Compression testing with the load applied parallel to the elongated struts showed a fracture strength of 356 MPa and a plastic strain of only 3.25% followed by a drop in stress of more than 30% which interrupted the testing. Although the struts had high aspect ratios, the plastic strain was lower than that of other foams with equiaxed pores; this was attributed to the sharp notches created by the elongated pores. Secondly, a Zr-based BMG structure ($p = 60\%$), processed by infiltrating an array of parallel W wire space-holders, resulted in a structure that had a high yield strength (820 MPa) but failed catastrophically at only 0.62% strain [8]. The high yield strength may be explained by the lack of stress concentrations created by the smooth, continuous, cylindrical pores oriented parallel to the axis of loading, and the initial fractures may have induced buckling of the continuous thin walls spanning the full height of the foam, leading to failure at low plastic strains. Finally, we reported on a Hf-based foam and a Zr-based foam with porosities of $p = 60\%$ and pores orientated ~26° to the direction of loading, which was processed using warm equal-channel angular extrusion (ECAE) of an amorphous and W space-holding powder blend [20,21]. The Hf-based foam had a peak stress of only 16 MPa due to incomplete bonding of the amorphous powders while the Zr-based foam had a yield strength of 61 MPa and showed compressive ductility of 60%. The increase in plastic strain in the Zr-based ECAE foam over the other two Zr-based and Ni-based foams may be attributed to the misalignment of struts with respect to the loading direction, allowing them to bend at multiple locations along their length, as is also observed in other BMG foams with equiaxed pores [22].

Here, we investigate this hypothesis by measuring the effect of pore orientation on the compressive properties of Zr-based BMG foams created by consolidating a blend of amorphous powders and W space-holder powders using ECAE. The resulting foams, which have highly aligned and elongated pores, are machined to produced samples with elongated pores oriented at angles of approximately 0°, 24°, 44°, 68° and 90° to the direction of loading.

2. Experimental procedures

Using a processing route described by Mathaudhu et al. [23], amorphous $Zr_{56.33}Nb_{5.14}Cu_{15.55}Ni_{12.92}Al_{10.03}$ powders (38–105 μm, fabricated at Ames National Laboratory by high-pressure gas atomization) were mixed with 60 or 70 vol.% crystalline W powders (45–106 μm). The powder blends were poured into $19 \times 19 \times 116\ mm^3$ nickel cans with a cylindrical cavity (11 mm in diameter and ~112 mm in height) which were plugged with a nickel insert and vacuum sealed by electron-beam welding. Electrodischarge machining was used to add a reference grid to one side of each can to visualize its deformation during extrusion. Lines were scored, ~0.5 mm deep, perpendicular to the extrusion direction at 50 mm intervals along the length of each can.

The sealed cans were then pushed at a rate of $0.13\ mm\ s^{-1}$ through a 90° ECAE die whose walls were heated to 430 °C with no counter-pressure. This temperature is within the BMG's supercooled liquid region, with glass transition and crystallization temperature $T_g = 415$ °C, $T_x = 460$ °C determined by differential scanning calorimetry of powders at $10\ K\ min^{-1}$. Each can was instrumented with one thermocouple along the can centerline, which, together with the tooling thermocouple, were used to monitor continuously the can temperature during extrusion.

After a single pass terminated by water quenching, compression samples ($\sim 3 \times 3 \times 6\ mm^3$) were electrodischarge machined from the densified composites in each can, with varying orientations to the shear plane created in the composite during extrusion. The deformed reference grid on the can was used as a guide to estimate the shear planes within the material. The resulting composite samples consisted of a $Zr_{56.33}Nb_{5.14}Cu_{15.55}Ni_{12.92}Al_{10.03}$ matrix containing elongated W powders (aligned along the shear direction) forming angles of approximately 0°, 24°, 44° and 68° with the long dimension of the sample (Fig. 1). One set of samples was cut with the long dimension in the y-direction, resulting in samples with the shear plane at an angle of 0° to the direction of loading and the powders aligned in the direction of shear at an angle of 90° to the direction of loading (sample marked 90° in Fig. 1).

Removal of the W phase from the composites, which was monitored by mass loss, required 100–125 h in an electrochemical cell with an aqueous solution of 1.5 M KOH

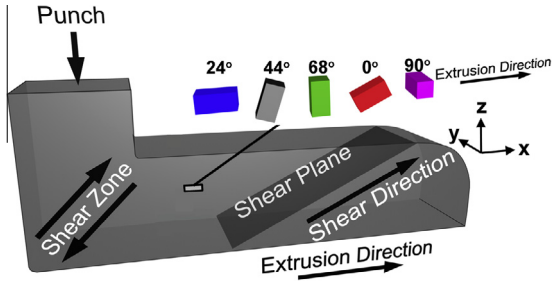

Fig. 1. Schematic of a can containing powders during ECAE processing showing samples machined from the center of the can to produce foams with pore orientation $\theta°$ to the direction of loading, where $\theta = 0°$ (red), 24° (blue), 44° (grey/black), 68° (green), 90° (magenta). (For interpretation of the references to color in this figure legend, the reader is referred to the web version of this article.)

operated at a voltage of 5.4 V. Before and after W dissolution, samples were coated with a thin layer of vacuum grease and their density and porosity was determined by the Archimedes method, where the sample mass is measured in air and in water. Attempts were made to process higher-porosity foams but composites with 75 and 80 vol.% W crumbled during W dissolution, probably due to incomplete mixing of the powders and limited deformation of the amorphous phase during extrusion.

To determine the mechanical properties of the foams, three specimens of each orientation were uniaxially compressed under displacement control at a nominal strain rate of $5 \times 10^{-4}\,s^{-1}$ using an MTS servohydraulic universal testing system. Stress was applied using hardened tool steel pistons with a lubricated steel sleeve acting as a compression cage ensuring parallelism; load train compliance corrections were made using data collected on an aluminum calibration standard before and after each test. The data are presented as engineering stress and strain, calculated from crosshead displacement after correction for load train compliance. After compression testing, a portion of each fractured sample was crushed and used for X-ray diffraction (XRD) using Cu K_α radiation.

3. Results

3.1. Microstructure

Fig. 2 shows scanning electron microscopy (SEM) micrographs of a *xz*-plane cross-section (sample surface parallel to the direction of extrusion, shown in Fig. 1) of the Zr-BMG/W composites from can 1 (60 vol.% W) and can 2 (70 vol.% W). These images show that good densification was achieved between and among the powders, together with extensive deformation of the W phase, resulting in an elongated morphology. Uneven mixing of the powders, which is evident in Fig. 2a where there are regions with high local content of the Zr-based phase (darker) and low content of the W phase (lighter), results in compression samples with a range of porosities. Optical micrographs of the foams (Fig. 3) after W phase dissolution show elongated pores with high surface area within a highly deformed amorphous matrix; however, some prior powder boundaries are visible in the matrix phase, indicating partial bonding of the amorphous powders.

SEM images of a foam from can 1 ($p = 45\%$, *xz*-plane cross-section) show extensive deformation and bonding of the Zr-based amorphous powders, which form a network of walls (Fig. 4) aligned in the direction of shear, forming a 22–28° angle with respect to the direction of extrusion. Prior powder boundaries are also visible in the network of elongated amorphous powders. Using SEM and optical micrographs, the pore orientation was measured to be at angles of $4 \pm 5°$, $24 \pm 4°$, $44 \pm 3°$, $68 \pm 5°$, $90 \pm 5°$ to the long axis of the sample (i.e. to the direction of compressive loading during testing).

The XRD patterns for the samples from both processed cans (Fig. 5) showed no measurable crystalline phases, confirming that no significant devitrification occurred during the powder consolidation step and that most of the W phase was removed during the electrochemical step. Chemical analysis (Wah Chang Co.) of a mechanically tested foam showed that only small amounts of W (0.71 wt.%) remain in the foam, possibly as rare isolated W powders

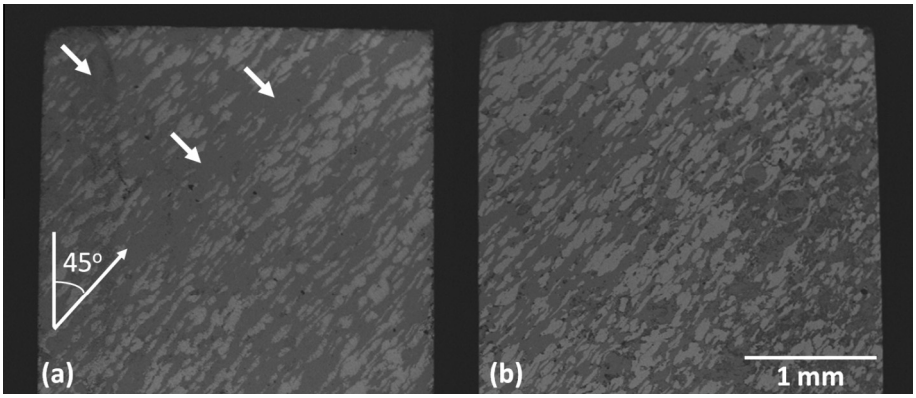

Fig. 2. SEM images of the *xz*-plane of the composite from (a) can 1 and (b) can 2, cut and polished with the material shear plane (and BMG elongated structures) at 44° to the direction of loading for the foams. Arrows indicate areas with high local fractions of Zr-based amorphous matrix (dark phase) in can 1.

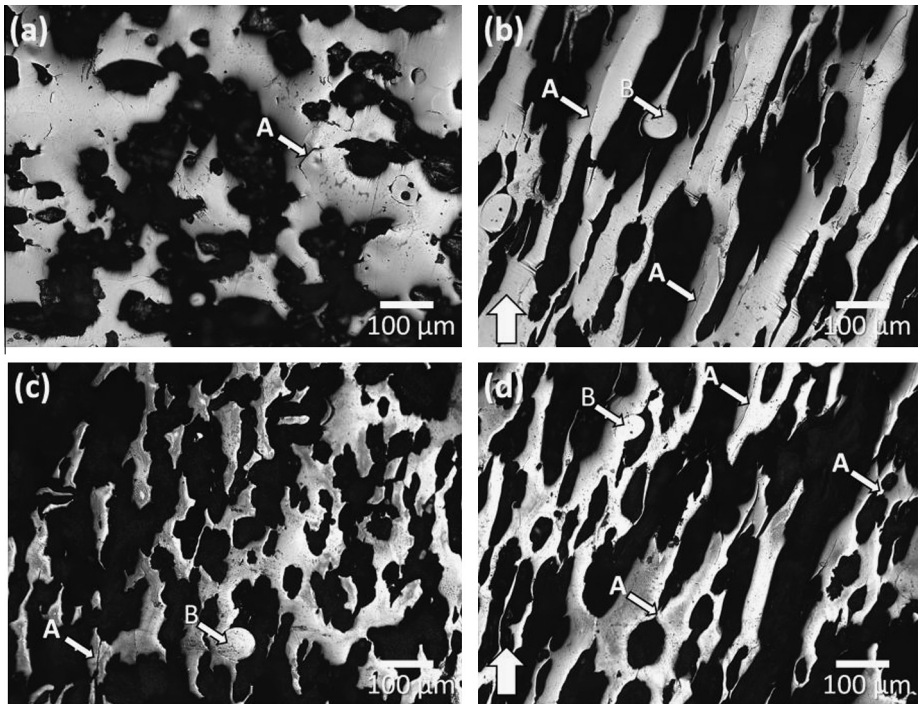

Fig. 3. Optical micrographs of cross-sections for the can 1 foam with the polishing plane (a) perpendicular and (b) parallel to the extrusion direction and for the can 2 foam with the polishing plane (c) perpendicular and (d) parallel to the extrusion direction. The thick white arrows indicate the direction of extrusion and the thin white arrows point to cracks at prior powder boundaries.

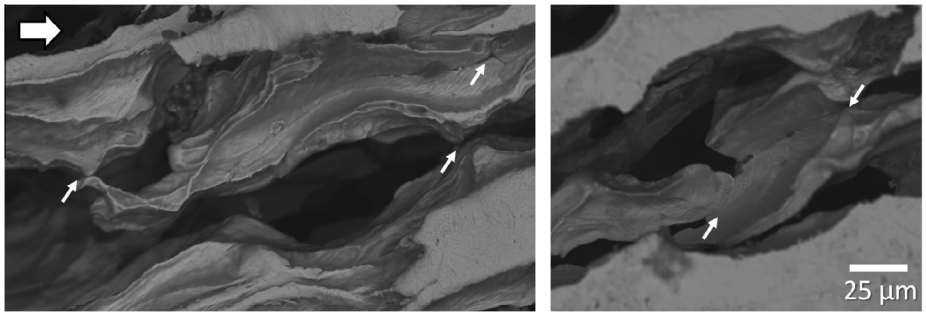

Fig. 4. SEM micrographs of the surface of Foam 24°/59%, before mechanical testing, with the polishing plane parallel to the extrusion direction (thick arrow). The thin arrows highlight incomplete powder bonding at prior powder boundaries.

that were not connected to the continuous W phase and hence not removed during the dissolution process.

3.2. Mechanical properties

3.2.1. 0° Orientation

Fig. 6a shows the engineering compressive stress–strain curves for three foams ($p = 37$, 45, 51%) with pores orientated ~0° to the direction of loading, referred to as Foam 0°/37%, 0°/45% and 0°/51%, respectively. The strongest specimen, Foam 0°/37%, exhibits a loading stiffness of 32 GPa and a peak strength of 319 MPa followed by a 236 MPa drop in stress corresponding to a large visible crack parallel to the direction of loading. The foam rapidly regained a stress capacity of 111 MPa, which was followed by a gradual decrease to a low 14 MPa plateau stress corresponding to the formation of additional cracks parallel to the direction of loading. As the strain increased, sheet-like sections of the sample detached from the bulk of the specimen (Fig. 7a) and ceased carrying load. The small serrations (dips and rises) in stress observed in the plateau region of the stress–strain curves (Fig. 6) are due to fractures in the load-bearing walls and the redistribution of load to other neighboring walls within the foam. The increase in load at 24% strain corresponds to the reloading of semidetached portions that had remained parallel to the direction of loading, and the increase in load at 40% strain corresponds to the collapse and reloading of detached portions. This is followed by densification at 60% stain, when the foam has completely collapsed and further strain on the contacting, collapsed walls results in compression of a nearly pore-free solid, leading to a rapid increase in stress.

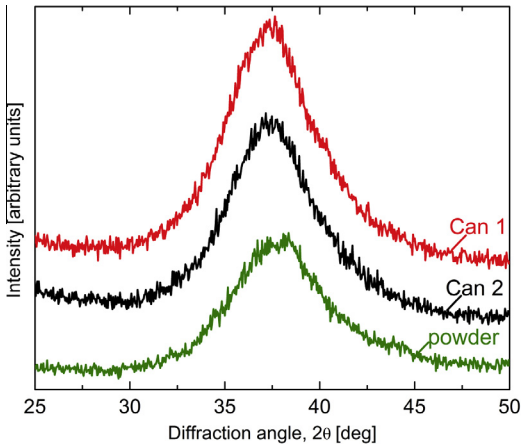

Fig. 5. XRD patterns of the foams from can 1 (60 vol.% W), can 2 (70 vol.% W) and the original powders showing a broad amorphous hump and no crystalline peaks.

Foams 0°/45 and 0°/51% exhibit loading stiffnesses of 21 and 12 GPa and peak strengths of 194 and 116 MPa, respectively, followed by a large drop in stress to a plateau of 1–5 MPa. Like Foam 0°/37%, these samples exhibited large cracks in the direction of loading and sheet-like sections of the sample split from the bulk. Unlike the stronger Foam 0°/37%, the splitting portions of these foams detached completely from the sample and stopped carrying load; at 35% strain Foam 0°/51% stopped carrying load (at which point the test was stopped) and Foam 0°/45% stress fell below 2 MPa. At higher strains, the detached portions of the latter sample were reloaded and the stress gradually increased to 30 MPa at 75% strain when the test was stopped.

3.2.2. 24° Orientation

Fig. 6b shows the stress–strain curves of samples with pore orientations ~24° to the direction of loading. These samples, Foams 24°/45%, 24°/58%, 24°/59%, had loading stiffnesses of 12, 4 and 3 GPa and peak stresses of 97, 31 and 21 MPa, respectively, followed by a ~50% drop in stress leading to a 30–75 MPa plateau region. At 7–9% strain, all three samples developed a single primary crack at an angle 23–26° to the loading direction, as shown in Fig. 7b for Foam 24°/45% (at 10% strain). The primary crack divides the samples into two sections with the upper portion shearing along the lower portion until the top section came in contact with the bottom platen at ~25% strain. At higher strains, additional cracks formed on parallel planes to the primary crack, forming a ~24° angle to the loading direction, and macroscopic shear was visible. Deformation for Foam 24°/58% was stopped at 12% strain to image the primary fracture surface, while Foams 24°/45% and 24°/59% were tested to the end of their plateau region, with densification starting at ~60% strain.

3.2.3. 44° Orientation

Fig. 6c shows the stress–strain curves of Foams 44°/38%, 44°/48% and 44°/49% which exhibit loading stiffnesses of 8, 4 and 4 GPa, respectively. These curves show a sharp stress drop after yielding (peak stresses of 87, 33 and 35 MPa, respectively) followed by a gradual increase in stress, leading to plateau stresses (106, 72 and 66 MPa, respectively) higher than the foam yield stress. The first visible crack was noted between 5% and 10% strain (Fig. 7c) and the number of cracks increased at higher strains. Macroscopic shearing of the sample was observed and, at 46% engineering compressive strain, Foam 44°/49% exhibited an average shear strain of $\gamma = \Delta w/h = 0.25$–$0.36$ (where h is the sample height and $\Delta w = 0.8$–1.2 mm is the lateral shear of the sample and was determined from photographs). At higher strains, after large macroscopic shearing, Foam 44°/38% began to form cracks that were not oriented parallel to the initial cracks and large portions of foam detached at higher strains, followed by densification at 60–65% strain.

3.2.4. 68° Orientation

As shown in Fig. 6d, unlike other pore orientations, the stress–strain curves of the foams with pores oriented 68° to the direction of loading do not show a sharp stress drop after yielding. The stress–strain curves are characterized by an elastic range followed by a gradual increase and then decrease in stress. Foams 68°/44%, 68/57% and 68/52% had loading stiffnesses of 2, 1 and 1 GPa and 0.2% yield stresses of 29, 14 and 17 MPa, respectively. Cracking is visible at a ~68° angle to the direction of loading between 5% and 10% strain and a crush band develops beneath the crack with the same orientation (Fig. 7d). Peak stress (93, 48, 19 MPa, respectively) was reached between 12% and 18% strain, followed by a gradual decrease in stress which corresponds to compression of and spalling from the crush band. A gradual increase in stress started at ~45% strain until rapid densification began at ~65% strain.

3.2.5. 90° Orientation

Fig. 6e shows the compressive stress–strain curves for samples with pores oriented 90° to the direction of loading and the shear plane parallel to the direction loading. Foams 90°/39%, 90°/48% and 90°/54% had loading stiffnesses of 18, 10 and 3 GPa, respectively. These compression curves are characterized by yielding (peak stresses of 146, 67 and 30 MPa, respectively) followed by a large drop in stress, corresponding to the formation of cracks with irregular paths through the width and height of the sample (Fig. 7e). As the strain increased, sections of the foam fully or partially detached from the bulk of the sample. At 15% strain, a large portion of Foam 90°/39% detached from the specimen, resulting in a large drop in stress. By 40% strain, Foam 90°/39% ceased carrying load and the detached portions of foam were pushed way from the sample with increasing strain. Foam 90°/48% carried only 1–3 MPa after initial yielding and the fractured portions of foam, still partially attached, were reloaded at 36% strain followed by densification starting at 70% strain. Large portions of Foam 90°/54% detached from the bulk of the

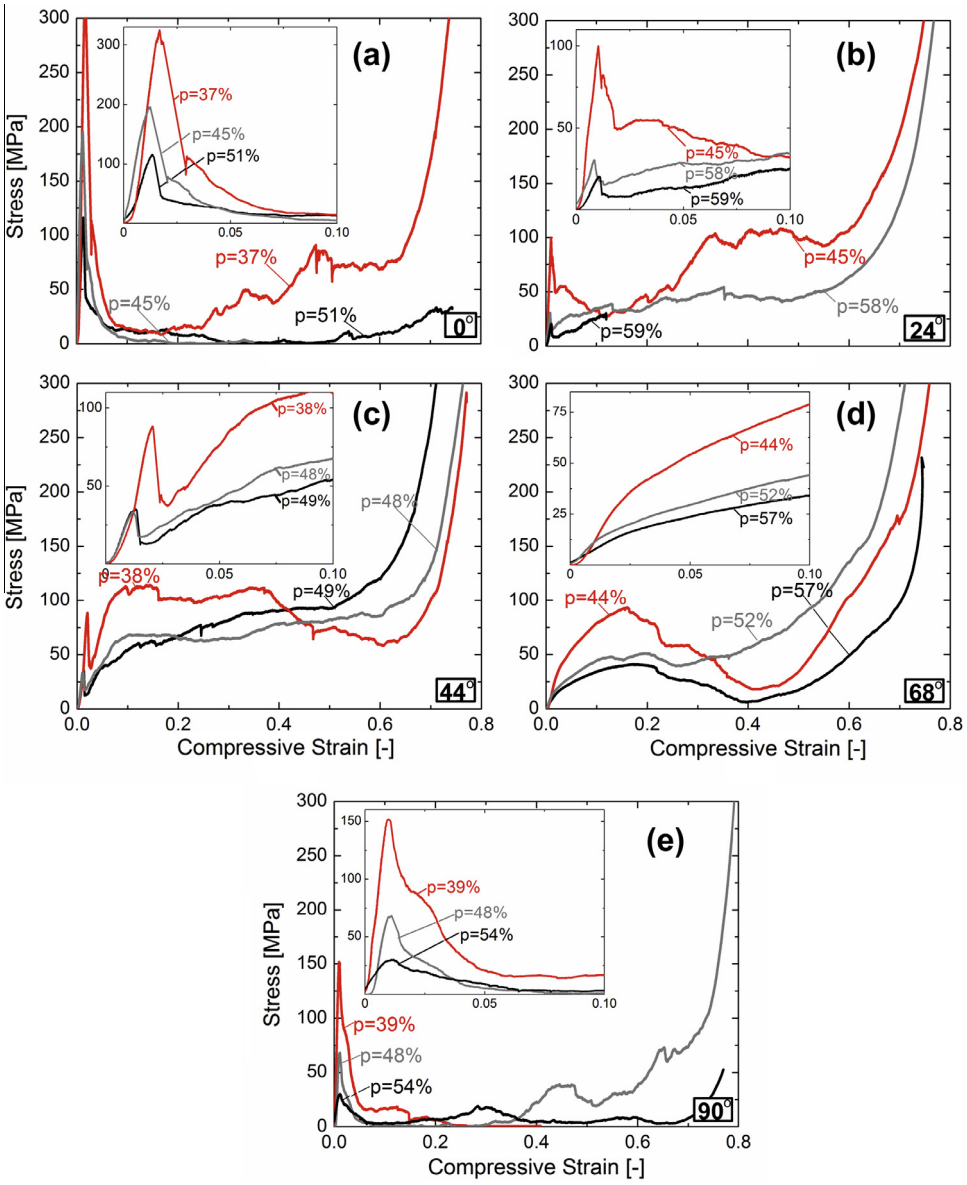

Fig. 6. Compressive stress–strain curves for foams with pore orientation of (a) ~0°, (b) ~24°, (c) ~44°, (d) ~68° and (e) ~90°, with respect to the loading direction. Each curve is marked with the porosity p of the specimen.

sample after yielding, leading to an average plateau stress of 7 MPa. As the strain increased, portions of the foam fractured from the sample and became non load-bearing; densification started at ~70% strain.

4. Discussion

4.1. Processing and microstructure

Processing procedures were slightly modified from those previously utilized [21,23] to accommodate the higher oxygen content and the smaller supercooled liquid region of the Zr-based amorphous powders used for the present foams. The Zr-based powders used here had an oxygen content of 0.144 wt.%, nearly twice that of the previously used Zr-based powders (0.078 wt.%). The decrease in the supercooled liquid region is attributed to the higher oxygen content [24] and the slightly different composition of the alloys ($Zr_{56.3}Nb_{5.1}Cu_{15.6}Ni_{12.9}Al_{10.0}$ vs. $Zr_{58.5}Nb_{2.8}Cu_{15.6}Ni_{12.8}Al_{10.3}$). To accommodate the higher glass transition temperature (from 403 to 415 °C), the processing temperature was increased from 420 to 430 °C; in addition, because higher oxygen contents are known to decrease bonding in conventional extrusion with area reduction [25], the rate of extrusion was decreased from 0.5 to 0.13 s^{-1} to promote bonding. Reductions in extrusions rates have been shown to improve homogeneous deformation during consolidation of Zr-based BMG powders using ECAE [26] which may promote the breakup of the oxide layer on the BMG powders, thus increasing bonding. Despite these modifications, prior powder boundaries are still visible in both optical and SEM images (Figs. 3 and 4), indicating

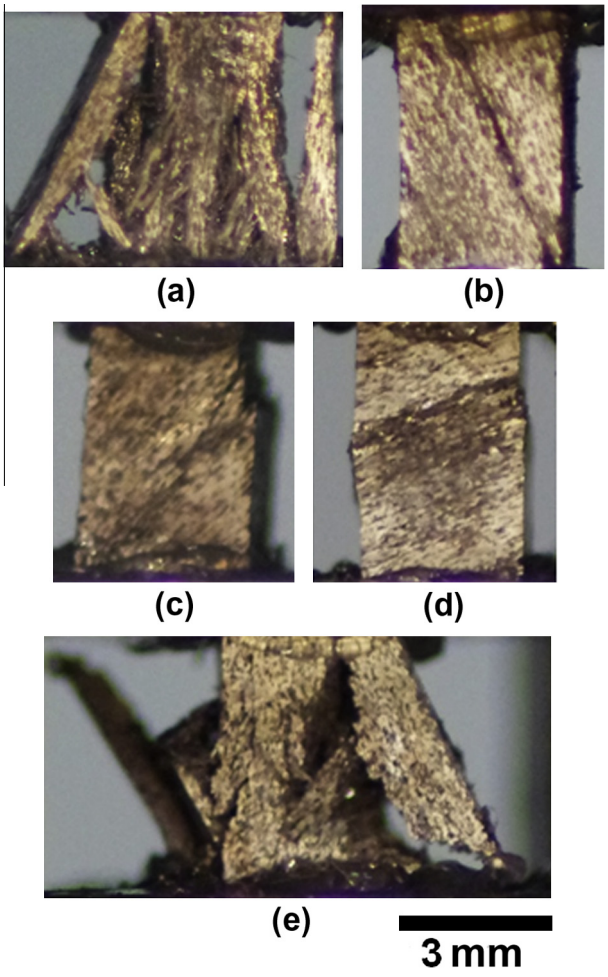

Fig. 7. Photographs of foams after 10% compressive strain: (a) Foam 0°/37%, (b) Foam 24°/45%, (c) Foam 44°/38%, (d) Foam 68°/44%, (e) Foam 90°/39%, showing cracks forming angles of (a) 0°, (b) 24°, (c) 44°, (d) 68° and (e) 90° with respect to the loading direction.

that the powders did not densify to the extent seen in previously processed foams using ECAE [21].

The presence of the prior powder boundaries in the current set of specimens underlines the importance of starting with low-oxygen, fully amorphous powders. The high-pressure gas atomization used to fabricate the base amorphous powders is sensitive to changes in the processing parameters and each batch should be monitored separately; however, the ability to process large quantities of low-oxygen amorphous powders has been demonstrated [21].

Unlike liquid-state processing techniques, which are very sensitive to processing temperatures, cooling rates and contamination of both the stock material and the processing environment [3], ECAE can accommodate less than ideal powders because of the flexible nature of processing within the supercooled liquid region of the amorphous materials. To improve repeatability, it is important either to use amorphous powders from the same batch or batches with similar oxygen contents.

As previously mentioned, uneven mixing of powders leads to regions of the composite with a high local content of one or the other phase (Fig. 2a), resulting in compression specimens with gradients of porosities and mechanical properties. While increasing the sample volume will improve the consistency of the specimen porosity, variation of porosity within the sample will still affect the foam's mechanical properties. A detailed study of the procedures used to blend and encapsulate the powders may improve powder distribution and lead to more uniform mechanical properties.

As discussed in a previous paper [21], powder densification during ECAE occurs through shear and hydrostatic stresses developed while the can is pushed through a 90° die angle. The shear plane is expected to form a 22° angle with respect to the direction of extrusion [27] although angle variations are expected because of wall friction and variation in tooling geometries [28]. Once the crystalline phase was removed, the SEM and optical images of the foams along the *xz*-plane show that the powders deformed along shear plane at a 20–28° angle with respect to the direction of extrusion.

The amorphous powders are highly deformed in the shear direction within the shear plane and deformed around the W powders, which also elongated in the shear direction. The large deformation in the shear direction leads to better bonding between powders in this direction. Significantly less deformation occurs in directions perpendicular to the shear direction, both within and perpendicular to the shear plane, leading to weaker (or no) bonding between the powders not in the shear direction. As a result, a network of highly elongated and well-bonded BMG powders is expected along the shear direction, with weaker connections between powders not in the shear direction.

4.2. Compressive behavior

Despite the wide range of porosities ($p = 35$–60%), which is known to affect strength and stiffness of foams, the stress–strain curves in Fig. 6 clearly indicate that pore orientation is also an important parameter.

For samples with 0° pore orientation, the foam is loaded parallel to the shear plane and shear direction created during ECAE. As previously discussed, matrix powders are highly elongated and well bonded in the direction of shear (and therefore loading direction). These well-bonded powders create a network spanning the height of the sample and are loaded in compression like columns, resulting in higher peak strengths (Fig. 8) and loading stiffness than any other pore orientation. However, after yielding, the stress drops dramatically as the few struts that bridge the crack shear planes fracture, resulting in low-energy-absorbing capabilities (Fig. 9), as determined from the area under the stress–strain curve for $p = 0$–60%. Fig. 10a shows the fracture surface of a sheet-like portion of foam that detached from Foam 0°/45% along the direction loading at low strain, like the detached sections of foam seen in Fig. 7a. Localized melting appears to have occurred toward the center of the fracture surface between two prior powder

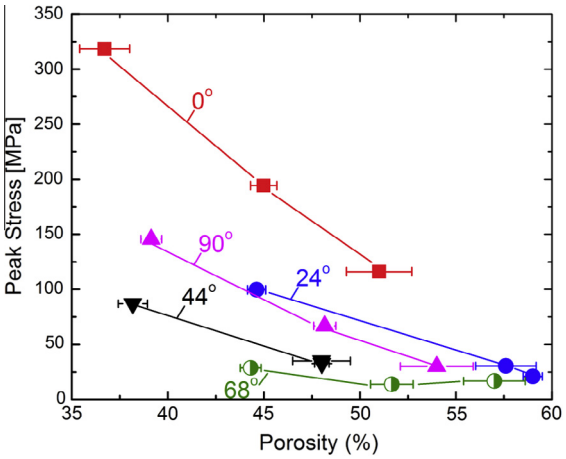

Fig. 8. Compressive peak stress as a function of porosity for foams with elongated pores at angles of approximately 0°, 24°, 44°, 68° and 90° with respect to the direction of loading. Values reported for Foam 68° samples are the 0.2% offset yield stress.

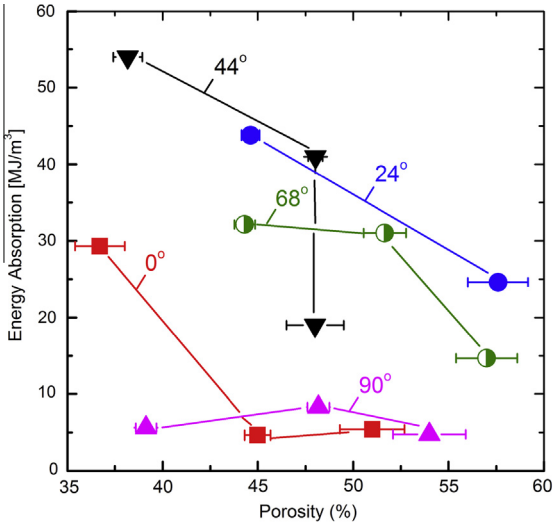

Fig. 9. Plot of energy absorbed during compression from $\varepsilon = 0$ to 60% as a function of porosity for various pore orientation.

boundaries, indicating that bonding was achieved between the powders which were sheared apart during testing.

A large drop in stress after yielding and reduced plastic strain has been observed in other BMG foams with highly elongated pores aligned to the direction loading, including the Zr-based honeycomb structure ($p = 60\%$) reported by Chen et al. [8]. This structure, which had a yield strength of 820 MPa, formed multiple shear bands that were arrested at the pores before catastrophic failure occurred at 0.62% plastic strain. The specific strength of this structure was $\sim$340 Nm g^{-1}, nearly 50% higher than the Zr-based foams with closed-cell, isotropic pores which have the next largest specific strength (217 Nm g^{-1} [9]) and 4–10 times the specific strength of the samples with 0° orientations reported here (35–76 Nm g^{-1}).

It has been noted that by Boccacini et al. [29] that cylindrical pores aligned perfectly with the direction of loading create no stress concentration. The foams presented here contain continuous pores that are not perfectly aligned and walls with uneven surfaces composed of bonded powders leading to increased stress concentrations, and therefore lower yield strengths. A low plastic strain value, $\sim$3.25%, in the Ni-based, extruded foam ($p = 40\%$) reported by Lee and Sordelet [19] was also attributed to increased stress concentration caused by sharp notches in the struts created during extrusion.

Foams with pores oriented 24° and 44° to the direction of loading both have stress–strain curves characterized by yielding followed by a drop in stress, a long plateau region and then densification. Both foams formed a primary crack that propagated through the sample along the shear plane in the shear direction, causing the sample to yield at lower stresses than the 0° orientation. Unlike the 0° orientation, fracture surfaces showed evidence of powder deformation and cracking without complete fracture as seen in the fracture surface of Foam 44° (Fig. 10b(A)) where a number of cracks initiate at a single point and branch into smaller, more diffuse cracks and shear bands. The beginning of a crack between a prior powder boundary elongated in the shear direction is visible and there is evidence of small cracks perpendicular to the powder boundary, indicating bending within elongated powder (Fig. 10b(B)). The 44° foam orientations loaded the elongated submillimeter walls in bending and, as predicted by Conner et al. [30] and observed in foams with equiaxed pores [17,18], non-catastrophic cracks and plastic deformation were observed, indicating some shear band stabilization and arrest. The accumulation of damage without catastrophic failure gives these foams better energy-absorbing capabilities (Fig. 9) than the other orientation.

Foams with pores oriented 68° to the direction of loading also had an elastic range that ended with the formation of a large primary crack; however, instead of a large stress drop corresponding to the shearing and detachment of significant portions of foam, this orientation formed a crush band characteristic of ductile foams after yielding. The peak stresses shown in Fig. 8 are the 0.2% offset values and are significantly lower than the other orientation and, unlike the 44° orientations, only small amounts of macroscopic shear were noted. Fig. 10c shows an example of cracking between prior powder boundaries formed in the shear plane between two powders elongated in the shear direction and shear bands formed on the surface of the lower powder. The loading of the walls in this orientation seems to promote wall deformation by plastic deformation of individual powders and fracture between powders. Damage/fracture was localized to a crushing band which increased this orientation's energy-absorbing capabilities (Fig. 9).

The foams with pores at an angle of 90° with respect to the loading direction and the shear plane at an angle of 0° with respect to the loading direction are similar to the Foam 0° samples since both have relatively large loading stiffness and high peak strengths (Fig. 8) followed by a

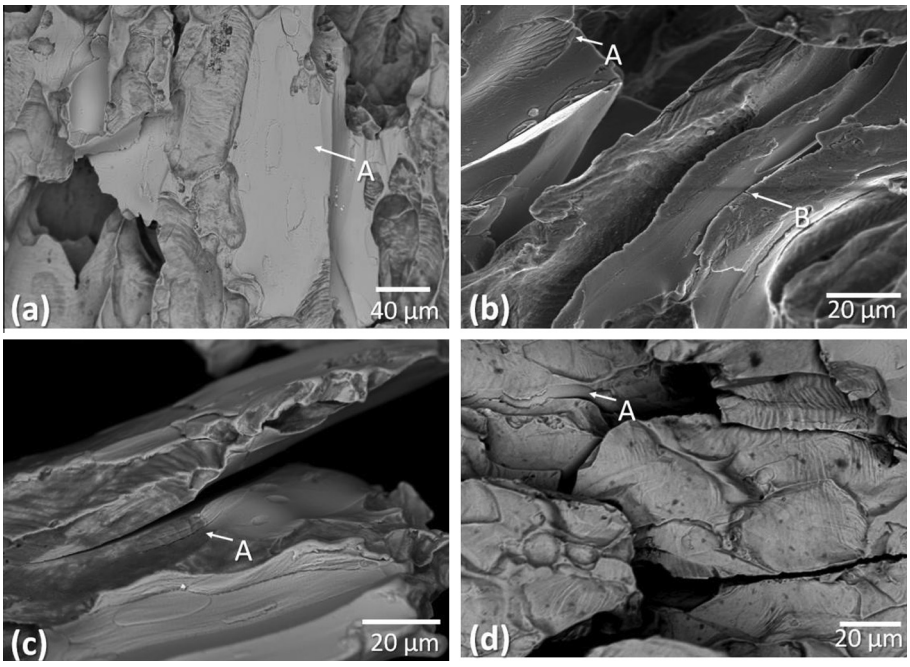

Fig. 10. SEM images of fracture surfaces for (a) Foam 0°/51%, where A indicates a fracture surface between two prior powders; (b) Foam 44°/49%, where A and B highlight non-catastrophic cracking within the prior powders; (c) Foam 68°/57 %, where A highlights shear band formation within a prior powder; and (d) Foam 90°/54%, where A highlights fractures at prior powder boundaries perpendicular to the shear plane.

large drop in stress resulting from the formation of many cracks in the sample. The walls loaded in the 90° foams are perpendicular to the shear direction but still within the shear plane. As previously discussed, these walls are formed by deformation around a W powder during densification, in a direction that is not subjected to strong shear forces during extrusion. Although these walls tend be perpendicular to the shear direction, there is no clear formation of long walls, like those observed within the shear direction. The 90° samples yield when cracks formed at prior powder boundaries oriented parallel to the direction of loading (perpendicular to the shear direction within the shear plane). Fig. 10d shows powders that separated by shear at prior powder boundaries. The individual powders did not show evidence of deformation. Although not as uniform as those formed in other orientations, cracks tend to run parallel to the direction of loading (Fig. 7) and large portions of sample detach from the specimen like the 0° orientation, leading to reduced energy-absorbing capabilities (Fig. 9).

4.2.1. Elastic modulus

4.2.1.1. Power law. The power-law formula is most often used to describe many physical properties of porous material with equiaxed pores [31]. The foam Young's modulus, E, is related to the Young's modulus of the bulk material, E_m, by:

$$E = E_m(1-p)^n \quad (1)$$

where p is the total porosity of the foam (expressed in dimensionless form), n is a geometric constant and $E_m = 86.7$ GPa (as reported for $Zr_{57}Nb_5Al_{10}Cu_{15.4}Ni_{12.6}$ [32]). The relative density for the foam is related to porosity by $1-p = \rho/\rho_m$, where ρ_m is the density of the bulk material and ρ is the density of the foam. Crystalline metal foams with lotus-type elongated, aligned pores and porosities <50% can be well described using Eq. (1) with empirical values of $n = 1$–1.2 for pores oriented parallel to the direction of loading and $n = 2.3$–3 for pores oriented perpendicular to the direction of loading [33–35].

Boccacini et al. [29] have suggested that the n-value is related to the stress concentrations that develop around a pore. Using 3-D elastic theory for stress concentrations around pores of various geometries, a value of $n = 2$ was found for spherical pores, $n = 1$ for long cylinders oriented parallel to the direction of loading (no stress concentrations effect), and $n = 3$ for cylinders aligned perpendicular to the direction of loading. These values match well with empirically determined values and the power-law relationship derived by Gibson and Ashby for foams that deform by strut bending. The Gibson–Ashby model predicts values of $n = 1$ for honeycombs loaded axially, $n = 3$ for honeycombs loaded in-plane, and $n = 2$ for isotropic pores [36].

These power-law predictions were developed for idealized structures where the pores do not interact with each other. Fig. 11a shows that these idealized power laws for $n = 1$ and $n = 3$ (cylinders aligned parallel and perpendicular to the direction of loading, respectively) greatly overestimate the moduli found for Foams 0° and 90°. The n-values in Eq. (1) were fitted to the measured moduli and porosities for each set of pore orientations, with the extremes being $n = 2.9$ and 5.9 for foams with 0° and 68°

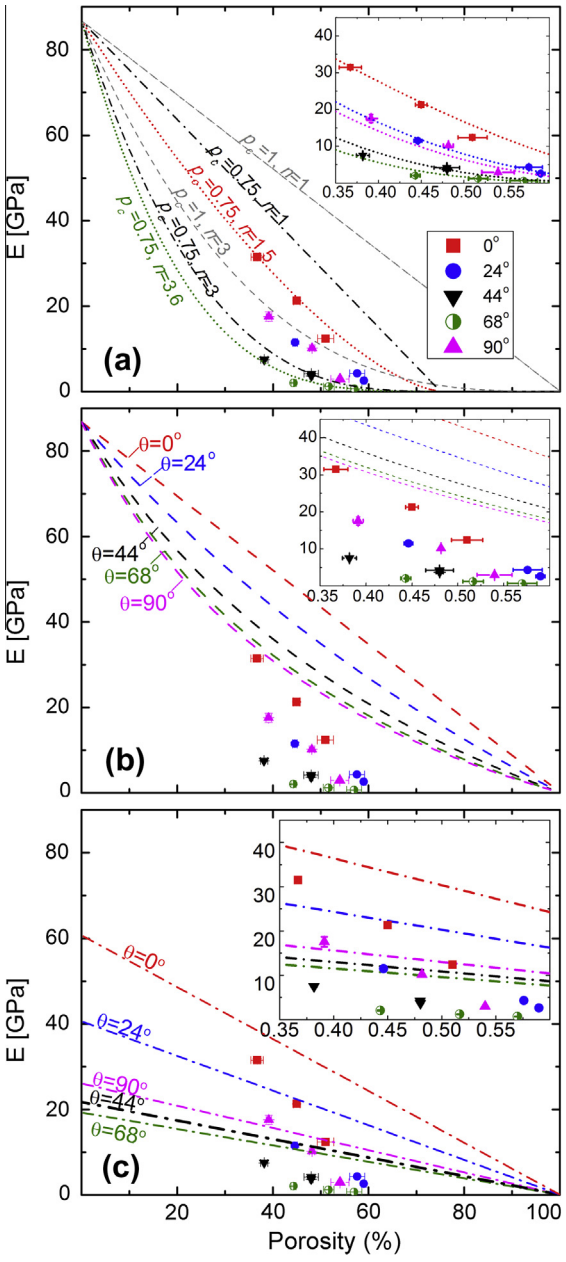

Fig. 11. Plots of foam stiffness as a function of porosity, showing experimental data points for foams with different loading orientations together with model predictions from (a) the analytical ($n = 1$ and 3) and empirical values ($p_c = 0.75$, $n = 1.5$–3.6) for power-law relationship Eq. (1) for material with elongated pores; (b) the Mori–Tanaka model for material with infinite cylindrical inclusions, Eq. (3); and (c) the truss model developed for wire woven square trusses, Eq. (4).

orientation, both above the predicted values. Although these values are high, their range encompasses the $n \approx 4$ found for materials containing pores with corner shapes [31].

For foams with $p > 30\%$ with open, interconnected, complex pore shapes, some researchers have used an effective porosity p_c which is the critical porosity at which the elastic modulus becomes zero and the foam fails immediately under any measurable stress. Phani [37] proposed the empirical relationship:

$$E = E_m\left(1 - \frac{p}{p_c}\right)^n \tag{2}$$

which maintains the boundary conditions ($p = 0$, $E = E_m$) for $p \leqslant p_c \leqslant 1$. Using $p_c = 0.75$ for the Phani model and $E_m = 86.7$ GPa [32], Fig. 11a shows that $n = 1$ still overestimates the modulus for the foams with a 0° orientation by 14–17 MPa, and $n = 3$ underestimates the modulus for the 90° orientation by 1–5 MPa while fitting the 44° and 68° orientations fairly well. Empirical values of $n = 1.6$, 2.1, 3.1, 3.6 and 2.4 are found for foams with 0°, 24°, 44°, 68° and 90° orientation fit, using Eq. (2) and $p_c = 0.75$ (Fig. 11a inset). These n-values are only slightly above the range predicted by Tane et al. [35]. These authors, using acoustic measurements of lotus-type porous iron ($p < 50\%$) to determine all the independent elastic constants, showed that the Young's moduli in an arbitrary direction can also be expressed by Eq. (1) with n-values of $n = 1.2$–3. It is interesting to note that the experimentally determined n-value for foams with a 90° orientation ($n = 2.4$) is smaller than the predicted $n = 3$. This may be attributed to the fact that the power-law equations are based on idealized foam geometries and/or the shear plane and the loading direction being parallel despite the fact that the shear direction (and therefore walls and pores) were oriented 90° to the direction of loading.

4.2.1.2. Mori–Tanaka model. Based on Eshelby's elasticity solution for inclusions in an infinite medium, the Mori–Tanaka model is used for composites with aligned inclusions (including fibers and spheroids). The Mori–Tanaka model can be used for porous materials by setting the inclusion stiffness to zero. The compliance tensor S of the specimen is given by [38]:

$$S = C_m^{-1} - p((C_f - C_m)(S_{cyl} - p(S_{cyl} - 1)) + C_m)^{-1}(C_f - C_m)C_m^{-1} \tag{3}$$

where C_m is the elastic stiffness tensor of Zr-based amorphous alloy (determined using a Young's modulus of 86.7 GPa, a Poisson's ratio of 0.38 found for amorphous $Zr_{57}Nb_5Al_{10}Cu_{15.4}Ni_{12.6}$ [32] and the assumption of isotropy), C_f is the stiffness tensor of the inclusions (taken as zero), S_{cyl} is the Eshelby tensor describing cylindrical inclusions, and I is the identity matrix. Solving Eq. (3) gives a stiffness matrix that can be rotated to find $E(\theta)$, where θ is the angle between the direction of loading and the shear plane. A θ rotation of the matrix $[S]$ about the 2-axis is performed by solving $[S'] = [R][S][R]^T$, where $[S']$ is the rotated compliance matrix, $[R]$ is the rotation matrix and the stiffness with the fibers oriented at an angle θ to the loading direction is $E(\theta) = 1/S'_{33}$ [39,40].

Fig. 11b shows that the Mori–Tanaka fiber model overestimates the loading stiffness by 20–30 GPa for all orientations in the porosity range of the foams tested. The Mori–Tanaka model assumes perfectly aligned cylindrical fibers

that do not interact, while the tested foams exhibit a network of pores that are preferentially elongated without being continuous or cylindrical, with pore intersections creating complex geometries leading to an increase in stress concentrations. Although the Mori–Tanaka model is an oversimplification of the foam geometry and does not take into account the imperfections in bonding of the ECAE foams, it captures the general trend of the effect of pore orientation on the loading stiffness (Fig. 12).

4.2.1.3. Square truss model. As previously discussed, the shear planes in the foams form highly elongated walls which span the width of the samples and the foam with 0° orientation exhibit such walls spanning the height of the sample. These elongated structures can be represented as a truss lattice. A metal textile truss lattices, for use in sandwich panel cores, was recently studied by Zupan et al. [41]. The out-of-plane modulus for a metal textile structure was found to scale linearly with porosity:

$$E = C_{el} \cdot E_m(1-p) \tag{4}$$

where $C_{el} = sin^4(\omega) = sin^4(90° - \theta)$, where ω is the angle between the faceplate and the wire truss, and θ is the angle between the truss and the direction of loading. For square lattice truss structures, $C_{el} = V_1\, sin^4(\omega_1) + V_2 sin^4(\omega_2)$, where ω_1 and ω_2 are the angles between the faceplate and the wires that make up the square lattice truss: $\omega_1 = \theta$ and $\omega_2 = 90° - \theta$. $V = V_1 + V_2$ is the volume fraction of trusses with an orientation of ω_1 or ω_2 that make contact with both the top and bottom faceplates (or platens). Unlike the woven wire model, the tested foams have trusses/walls that can transfer load to neighboring trusses. To estimate the V_1 and V_2 values, the optical micrographs of the 0° and 24° foams' *xz*-plane cross section (like those in Fig. 3b and d) were analyzed and the number of elongated walls in the shear direction and the number of walls perpendicular to the shear direction were counted, resulting in 62–75% of the cell walls aligning in the shear plane. Fig. 11c shows that the truss model, for $V_1 = 0.7$, $V_2 = 0.3$, $\omega_1 = \theta$ and $\omega_2 = 90° - \theta$, overestimates the loading stiffness of the foams by ~8–15 GPa, a significant improvement over the Mori–Tanaka model. The effect of wall orientation on the loading stiffness is also more accurately reflected in this truss model, as there is an increase in stiffness as θ approaches 90° reflecting the loading of the walls perpendicular to the shear plane (Fig. 12). The truss model can only be applied to foams with high porosities and highly elongated walls as the model assumes trusses with large aspect ratios (wires) and does not fulfill the boundary condition requirement for $p = 1$ resulting in $E = E_m$.

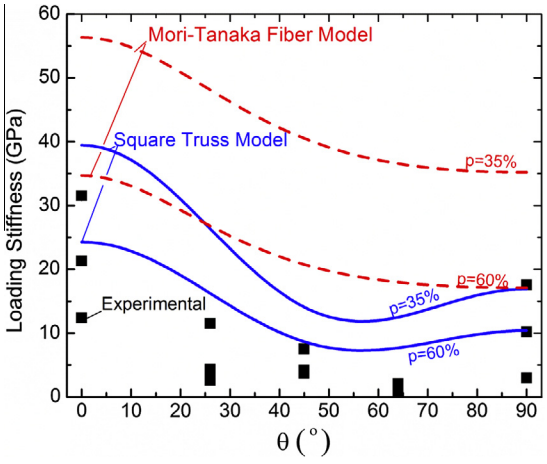

Fig. 12. Plot of foam stiffness as a function of pore orientation with respect to the loading direction for foams with porosities $p = 37$–59% showing experimental data points and predicted values using the Mori–Tanaka fiber model (Eq. (3)) and the square truss model (Eq. (4)).

5. Conclusions

The orientation of the highly aligned and elongated walls that compose $Zr_{56.3}Nb_{5.1}Cu_{15.6}Ni_{12.9}Al_{10.0}$ BMG foams produced by elongated W space-holder removal from a BMG/W composite has a marked affect on the mechanical properties of these materials. An increase in the compressive plastic deformation of the foams can be achieved via bending of walls and cracking between prior powder boundaries by misaligning the walls and the loading direction. Increasing the plastic deformation by misaligning the walls (24–68° to the direction of loading) increases the compressive ductility and energy absorption. Aligning the walls parallel or perpendicular to the direction of loading increases the peak strength of the sample but results in low compressive ductility and energy-absorbing capabilities. Simple analytical models overestimate the Young's modulus of the foams, most likely because the models do not account for imperfections present in the real foams. However, all of the models capture the general trend of decreasing stiffness with increasing porosity and increasing misalignment between the elongated pores and the loading direction. The square truss model also captures the observed increase in stiffness when the pores are oriented perpendicular to the direction of loading.

Acknowledgments

M.E.C. was supported by a National Science Foundation Graduate Research Fellowship. This work was funded by the Army Research Laboratory (ARL) and the authors thank Drs. Laszlo Kecskes and Suveen Mathaudhu (ARL) for useful discussion and Mr. Micah Gallagher (ARL) for assistance in machining samples. The authors also thank Mr. Larry Jones at Ames Laboratory (Department of Energy) for BMG powder preparation; they acknowledge useful discussions with, and use of the ECAE equipment of, Prof. K. Ted Hartwig (Texas A&M University, TAMU) as well as the experimental assistance of Mr. Robert Barber and Mr. David Foley (TAMU) in operating the equipment.

References

[1] Schuh CA, Hufnagel TC, Ramamurty U. Acta Mater 2007;55:4067.
[2] Park ES, Kim DH. Met Mater Int 2005;11:19.
[3] Brothers AH, Dunand DC. Scripta Mater 2006;54:513.
[4] Brothers AH, Dunand DC. Adv Mater 2005;17:484.
[5] Schroers J, Veazey C, Johnson WL. Appl Phys Lett 2003;82:370.
[6] Wada T, Inoue A. Mater Trans 2004;45:2761.
[7] Brothers AH, Scheunemann R, DeFouw JD, Dunand DC. Scripta Mater 2005;52:335.
[8] Chen XH, Zhang Y, Zhang XC, Hui XD, Wei BC, Chen GL. Electrochem Solid-State Lett 2007;10:E21.
[9] Wada T, Wang X, Kimura H, Inoue A. Scripta Mater 2008;59:1071.
[10] Demetriou MD, Duan G, Veazey C, De Blauwe K, Johnson WL. Scripta Mater 2007;57:9.
[11] Jayaraj J, Park BJ, Kim DH, Kim WT, Fleury E. Scripta Mater 2006;55:1063.
[12] Gebert A, Kundig AA, Schultz L, Hono K. Scripta Mater 2004;51:961.
[13] Lee MH, Sordelet DJ. Scripta Mater 2006;55:947.
[14] Brothers AH, Dunand DC, Zheng Q, Xu J. J Appl Phys 2007;102.
[15] Ide T, Tane M, Ikeda T, Hyun S, Nakajima H. J Mater Res 2006;21:185.
[16] Wada T, Kinaka M, Inoue A. J Mater Res 2006;21:1041.
[17] Brothers AH, Dunand DC. Acta Mater 2005;53:4427.
[18] Demetriou MD, Veazey C, Harmon JS, Schramm JP, Johnson WL. Phys Rev Lett 2008;101:145702.
[19] Lee MH, Sordelet DJ. Appl Phys Lett 2006;89:021921.
[20] Cox ME, Kecskes LJ, Mathaudhu SN, Dunand DC. Mater Sci Eng A 2012;533:124.
[21] Cox ME, Mathaudhu SN, Hartwig KT, Dunand DC. Metall Mater Trans A 2010;241:1706.
[22] Brothers AH, Prine DW, Dunand DC. Intermetallics 2006;14:857.
[23] Mathaudhu SN, Hartwig KT, Karaman I. J Non-Cryst Solids 2007;353:185.
[24] Lin XH, Johnson WL, Rhim WK. Mater Trans JIM 1997;38:473.
[25] Kawamura Y, Kato H, Inoue A, Masumoto T. Int J Powder Metall 1997;33:50.
[26] Karaman I, Robertson J, Im J, Mathaudhu SN, Hartwig KT, Luo Z. Metall Mater Trans A 2004;35:247.
[27] Segal VM. Mater Sci Eng A 1995;197:157.
[28] Oh SJ, Kang SB. Mater Sci Eng A 2003;343:107.
[29] Boccaccini A, Ondracek G, Mombello E. J Mater Sci Lett 1996;15:534.
[30] Conner RD, Li Y, Nix WD, Johnson WL. Acta Mater 2004;52:2429.
[31] Ji S, Gu Q, Xia B. J Mater Sci 2006;41:1757.
[32] Choi-Yim H, Conner RD, Szuecs F, Johnson WL. Acta Mater 2002;50:2737.
[33] Ichitsubo T, Tane M, Ogi H, Hirao M, Ikeda T, Nakajima H. Acta Mater 2002;50:4105.
[34] Hyun SK, Nakajima H. Mater Sci Eng A 2003;340:258.
[35] Tane M, Ichitsubo T, Nakajima H, Hyun SK, Hirao M. Acta Mater 2004;52:5195.
[36] Gibson LJ, Ashby MF. Cellular solids: structure and properties. 2nd ed. Cambridge: Cambridge University Press; 1997.
[37] Phani KK, Niyogi SK. J Mater Sci 1987;22:257.
[38] Qu J, Cherkaoui M. Fundamentals of micromechanics of solids. New York: Wiley; 2006.
[39] Neurohr AJ, Dunand DC. Acta Mater 2011;59:4616.
[40] Daniel IM, Ishai O. Engineering mechanics of composite materials. 2nd ed. Oxford: Oxford University Press; 2005.
[41] Zupan M, Deshpande VS, Fleck NA. Eur J Mech – A/Solids 2004;23:411.